The Quasi-Solid Box Method for Simulating Wind Around Obstacles in the System for Atmospheric Modeling

Marat F. Khairoutdinov[1], Andrew M. Vogelmann[2], and Katia Lamer[2]

[1] School of Marine and Atmospheric Sciences, Stony Brook University, Stony Brook, New York, USA
[2] Brookhaven National Laboratory, Upton, New York, USA

Key points:

- A simple modification to the anelastic equations in the System for Atmospheric Modeling enables explicit resolution of the flow around buildings.
- The accuracy of the methodology is demonstrated using single-building wind tunnel data.

Abstract

A novel method to represent the flow around obstacles such as buildings is developed and incorporated into the System for Atmospheric Modeling (SAM). The Quasi-Solid Box Method (QSBM) introduces a simple modification to the anelastic equations that forces the flow to stagnate within the obstacle's boundaries. The performance of the modified SAM is evaluated using CEDVAL (Compilation of Experimental Data for Validation of Microscale Dispersion Models) wind tunnel measurements of the wind and tracer dispersion around a single rectangular building. All major flow features are well simulated, such as the arch vortex leeside of the building, height of the flow separation point in front of the building, "separation bubbles" over the rooftop and on building sides, and leeside return flow towards the building. The dispersion of the tracer released at the building base is also simulated quite reasonably. To demonstrate the ability of the method in more general cases when buildings boundaries do not conform to the grid-cell boundaries, we report results for successful simulation of a flow around a cubic building rotated by 45^{o} relative to the flow, and around a building in the form of a cylinder of aspect ratio of one. The QSBM has virtually no additional computational cost and can be implemented in any anelastic model.

Corresponding author: Marat Khairoutdinov, marat.khairoutdinov@stonybrook.edu

Plain Language Summary

A novel method to simulate the wind and turbulence around obstacles, such as buildings, has been developed for use in a computer model that was previously used only to study turbulence and clouds over flat Earth surface. The method, called the Quasi-Solid Box Method, forces the simulated flow to stop in the model grid-cells that are inside an obstacle. The accuracy of the method is tested using cases of a flow past an idealized single rectangular building, a cubic building rotated by 45^o, and a building in the form of a cylinder. The simulations are compared with wind tunnel observations around a small model building and to results from other models. The modeled gas tracer dispersion around the building also agrees quite well observations. We also report results for successful simulation of a flow around a cubic building rotated by 45^o relative to the flow, and around a building in the form of a cylinder of aspect ratio of one. The main appeal of the new method is its simplicity that requires very minor modifications to the model code. The improved model can be used for detailed studies of the impact of climate change on urban environments.

1. Introduction

Predicting how climate change will impact the Earth's climate system is a longstanding goal that has motivated the development of an array of global climate models. Historically, climate models have been focused on predicting how climate change will impact natural environments. As 55% of the world's population now lives in cities (Profiroiu et al., 2020), there has been growing interest in understanding how climate change will impact human stress as well and also how urban features themselves affect the stress level. Urban environments are visibly complex with their mix of land use and array of surface types. The high-level of heterogeneity and small scale of urban elements further motivates the general trend towards developing higher-resolution models.

The System for Atmospheric Modeling (SAM; Khairoutdinov & Randall, 2003) is a computationally efficient model that has been widely used within the community to study atmospheric processes. Its computational efficiency comes from the use of the anelastic approximation to the momentum equations and is fully scalable to run as a cloud-resolving model at kilometer resolutions down to only a few meters as a large-eddy simulation model. This high degree of scalability presents an opportunity to simulate climate impacts on urban microclimates down to street-resolved resolutions. Such simulations, however, require an efficient way to represent heterogeneous urban landscapes and, particularly, how they affect wind flow and transport within streets and around buildings. Winds are chosen as a starting point as they act to ventilate heat, moisture and gas tracers and disperse of airborne contaminants. This paper provides a computationally efficient framework to make simulations building-aware in anelastic models such as SAM.

There are various methods for incorporating the impact of obstacles on wind flow in atmospheric models. The terrain-following coordinate transformation method (Gal-Chen & Somerville, 1975) has been used in many atmospheric models to incorporate the terrain. Unfortunately, its application may encounter some problems; for example, pressure gradient forces along a curved coordinate can lead to spurious flows at high model resolutions near steep terrain (e.g., Fortunato and Paptista, 1996). More importantly though, its application in SAM would require abandoning the use of the non-iterative bidirectional Fast Fourier Transform (FFT) solver for Poisson equation for pressure (which would include cross-derivatives), resulting in reduced computational efficiency and the need for development of an iterative elliptic equation solver.

There are other methods to modeling a flow past obstacles, such as buildings, in the computational fluid dynamics (CFD) community. One is to generate a curvilinear structured or unstructured grid that conforms to the obstacle's outer boundaries (e.g., Hanna, 2006; Blocken, 2018). However, in this case, modeling a different set of buildings would require generation of an entirely different grid. Local grid refinement would also be typically used to better resolve the flow near an obstacle's boundaries, especially when a building has a complex shape with many sharp edges. Arguably, this is the most comprehensive approach, but it may be quite complicated and computationally expensive, with complex grid-generation techniques that minimize the skewness of the resultant grids. Another popular method is the Immersed Boundary Method (IBM). In the IBM, the grid does not necessarily conform to the obstacle's outer boundaries and can be, for example, a regular Cartesian grid. For this method, an accurate algorithm is also needed to determine exactly where the buildings' surfaces lie relative to the specified grid. Then, carefully crafted forcing terms are added to the model momentum equations to force the velocity to be tangential to the projected surface of an obstacle (e.g., Iaccarino and Verzicco, 2003; Mittal & Iaccarino, 2005). The advantage of the IBM is that the obstacle's actual boundaries are captured as opposed to being truncated by the grid cell boundaries. Also, for moving obstacles, the grid does not have to change; only the boundary's current position should be recomputed. The IBM has been used in atmospheric models to simulate flow over terrain (Lundquist et al., 2010), blunt objects, and buildings in the atmospheric boundary layer (e.g., Lundquist et al., 2010; Kumar and Tiwari, 2021). However, implementing the IBM in SAM would not only require abandoning the FFT solver for the pressure equation, but it would also involve performing careful interpolation of the velocity flow at each time step, and possibly local grid refinement, to improve accuracy. As a result, it would lead to considerable code modifications and may generate complications arising from the requirement that, in the anelastic equations used in SAM, the predicted momentum field must be non-divergent at the end of each time step.

In one of the variants of the IBM, sometimes called the "body-force method", the flow is not forced to be tangential to the projected building surface but, rather, fictitious nudging terms are used to force the velocity of the flow inside the obstacle to stagnate over a time horizon comparable to the model time step (Chen & Leach, 2007; Smolarkiewicz et al., 2007; Korycki et al. 2016; Muñoz-Esparza et al., 2020). An advantage of the body-force method is that it can also be used to represent porous obstacles such as trees. The nudging time scale is usually chosen to be inversely proportional to the wind velocity; as such, in high wind conditions the model time step may have to become very small for stability of the time integration scheme, which results in increase computational expense.

In this study, we propose and test a variant of the "body-force method", which we call the Quasi-Solid Box Method (QSBM). In principle, the QSBM can be applied to any anelastic or Boussinesq model. The method allows one to halt the flow almost completely inside a chosen group of cells comprising an obstacle, and it does not require any explicit nudging terms. Also, the method does not impact the integration time step, which remains bounded by the usual Courant–Friedrichs–Lewy (CFL) stability constraint which is based on the resolved velocity already in SAM. The practical advantage of the QSBM is that it is very simple and requires very minor code changes; further, the FFT solver for the pressure equation does not require any modifications, thus preserving SAM's computational efficiency.

The main drawback of the QSBM is that it requires approximation of an obstacle's shape by using only whole grid cells; this may create staircase-like boundaries for otherwise smooth boundaries that do not conform to the model grid, which may create additional noise and turbulence. However, this potential, additional turbulence is not considered to be of concern for the intended application of this method in SAM which is to simulate the flow and tracer transport around a city that is already immersed in a highly turbulent atmospheric boundary layer. This is fortunate as a rather coarse resolution is available to represent the many individual buildings within the city without incurring an enormous computational cost. We note that the real buildings, unlike many idealized models of buildings used in wind-tunnel experiments, have many irregular surface features—such as window cavities, balconies, architectural add-ons—that usually are not well represented by computer models anyway, but which can also produce turbulence. In addition, the turbulent flow in the boundary layer around real buildings itself is not very well resolved at small scales, even when large-eddy simulation (LES) is used. Within the context of the flow around the whole city, it is not clear how important all these details of the buildings (inherently unresolved by any LES) actually are to generating additional turbulence, which would require additional research in the future.

This paper is organized as follows. Details regarding the implementation of the QSBM in SAM are described in Section 2. A demonstration of the performance of the QSBM is provided in Section 3 where we compare an LES of the flow past a single rectangular building against wind-tunnel measurements. In this case, the building orientation is such that its boundaries ideally conform to the Cartesian grid's cell boundaries. Therefore, in Section 4, we also demonstrate the generality of the method through results for two additional simulations of the flow around obstacles with the boundaries that do not conform to the grid cell boundaries. The first case is the flow around a cubic building rotated 45^{o} to the direction of the flow, and the second case is the flow around a building in the form of a circular cylinder. A summary of the results is provided in Section 5.

2. The Quasi-Solid Box Method (QSBM)

Prognostic velocities in anelastic models, like SAM, cannot be simply set to zero at the boundaries of cells inside obstacle at the end of each time step because it would violate the non-divergence equation and lead to noise and numerical instability; thus, we design a method to produce a similar result. Like in the body-force method, the proposed QSBM adds a simple Newtonian damping nudging term to the momentum equations:

$$\frac{\partial \boldsymbol{u}}{\partial t} = \boldsymbol{A} - \nabla\pi - \frac{\boldsymbol{u}}{\tau} \tag{1}$$

where $\boldsymbol{u}$ is the velocity vector, $\nabla\pi$ is the pressure gradient, τ denotes a damping time scale, and $\boldsymbol{A}$ denotes all other terms like advection, diffusion, Coriolis force, etc. One can see that the damping term forces the wind to decelerate and eventually stop over some time. For the Arakawa-C grid, this damping term is activated for all the velocity components at the sides of each cell located inside an obstacle; otherwise, no damping is applied.

To reproduce the effect of wind stopping abruptly at the face of an obstacle, τ in (1) should be infinitesimally small. However, since SAM uses the explicit third-order Adams-Bashforth (AB3) scheme for time integration, the minimum allowed value for τ is approximately two time-steps for a non-oscillatory solution (Duran, 1991); otherwise, the computations would be unstable or oscillatory. As damping to near zero would take at least a time interval of 3 τ, or about six time-steps, it is obvious that such damping would be of no practical use—the flow would easily penetrate deep into the obstacle before stagnating; or, in the case of a relatively small obstacle, even go right through it. Therefore, a much smaller damping time scale is required.

One way to avoid numerical instabilities while introducing damping terms to the velocity acceleration terms is to use an implicit scheme as follows. First, the provisional wind field $\boldsymbol{u}^*$ is obtained using only the $\boldsymbol{A}$ terms:

$$\boldsymbol{u}^* = \boldsymbol{u}^n + \Delta t^n (a\boldsymbol{A}^{n-1} + b\boldsymbol{A}^{\boldsymbol{n-1}} + c\boldsymbol{A}^{n-2}) \qquad (2)$$

where a, b, and c are AB3 coefficients that depend on the current time step Δt^n and past time steps Δt^{n-1} and Δt^{n-2}. Next, the implicit correction to the provisional solution is made to include the damping term:

$$\boldsymbol{u}^{**} = \boldsymbol{u}^* - \boldsymbol{u}^{**}\frac{\Delta t^n}{\tau} \qquad (3)$$

noting here that the implicit approximation (3) is computationally stable for any value of τ. Equation (3) can be rewritten as

$$\boldsymbol{u}^{**} = \boldsymbol{u}^* \frac{1}{1+\frac{\Delta t^n}{\tau}} \qquad (4)$$

This form makes it easy to see that in the limiting case where flow comes to a complete stop at the obstacle boundary for $\tau = 0$, or *instantaneous* relaxation, the factor $\frac{1}{1+\frac{\Delta t^n}{\tau}}$ becomes zero too. Given this, it is sufficient to require that the *corrected provisional velocity* $\boldsymbol{u}^{**}$ *be zero at all sides of the cells inside an obstacle,* i.e.,

$$\boldsymbol{u}^{**} = 0 \quad \text{at all sides of cells inside an obstacle} \qquad (5)$$

and there is no need to specify a value for τ. Note, however, that representing the flow through porous obstacles such as bushes and trees would require setting some explicit value to the relaxation time-scale τ in (4). The final solution can then be obtained by performing the pressure-correction step

$$\boldsymbol{u}^{n+1} = \boldsymbol{u}^{**} - \Delta t^n (a\nabla\pi^n + b\nabla\pi^{n-1} + c\nabla\pi^{n-2}) \qquad (6)$$

where π^n is unknown and should be obtained from the solution of an elliptic equation following

$$\nabla(\rho\nabla\pi^n) = \frac{1}{\mathrm{a}\Delta t^n}\nabla\cdot\rho\boldsymbol{u}^{**} - \frac{b}{a}\nabla(\rho\nabla\pi^{n-1}) - \frac{c}{a}\nabla(\rho\nabla\pi^{n-2}) \qquad (7)$$

which is derived using the mass continuity constraint on the final velocity field:

$$\nabla \cdot \rho \boldsymbol{u}^{n+1} = 0 \tag{8}$$

It is important to realize that requiring $\mathbf{u}^{**}$ to be zero at all sides of the cells inside an obstacle does not automatically mean that the final velocity $\boldsymbol{u}^{n+1}$, obtained from the pressure correction (6)-(7), will also be exactly zero; this is due to the inherently non-local nature of the elliptic equation for which the solution at a particular point depends simultaneously on the solution for the whole grid. However, as will be shown in Section 3d, the velocity field inside the obstacle is very small compared to the velocities right outside it. This outcome is explained by the fact that the pressure correction to the provisional velocity $\boldsymbol{u}^{**}$, to enforce continuity at each time step, is generally small. This is because the velocity change over a single time step is generally small, causing only a small divergence of the provisional momentum field to develop, which is precisely non-divergent at the beginning of each time step. The suppression of velocity inside obstacles can be further improved by iterating steps (5)-(7), which would make the final velocity $\boldsymbol{u}^{n+1}$ after the pressure correction be a new provisional velocity $\boldsymbol{u}^{*}$ to obtain the total solution (note that the solutions for pressure at each additional iteration should be added to the solution at previous iteration). Each additional iteration would add some additional computational expense to solving the elliptical equation (7). Obviously, the additional iterations only improve the solution inside the obstacles or near them and do not have any effect on the solution when obstacles are not present. As will be demonstrated in this study, the existence of small residual velocities does not seem to affect the simulated flow outside the obstacle in any significant manner; therefore, the iterations may not be even needed in most cases. This notion is consistent with results by Chen & Leach (2007), who compared an accurate solid-building approach to a simplified approach in which buildings are modeled by nudging the velocity to zero. A rather significant resultant nonzero residual flow occurred inside the buildings, but they also found a relatively small effect of such approximation on the external flow. Note that in some more traditional and accurate IBM approaches applied to anelastic or incompressible models, an expensive elliptic equation also needs to be solved at least twice on each time step (e.g., Zhang and Zheng, 2007).

3. Simulation of the flow around rectangular building

To test the performance of the QSBM in simulating the flow around solid obstacles, we performed two LES simulations for the case of a single rectangular building and compared it to the observational dataset from the Compilation of Experimental Data for Validation of Microscale Dispersion Models (CEDVAL; https://mi-pub.cen.uni-hamburg.de/index.php?id=433). We use reference cases from A1-1, which have been previously used for evaluation of other numerical models (e.g., Diehl et al., 2007; Gorlé et al., 2010; Trini Castelli & Reisin, 2010; Parente et al., 2011; Zhang et al., 2016). Specifically, we will use A1-1 to evaluate the velocity field and A1-5 to evaluate the dispersion of a gas tracer.

a) Case setup

The A1-1 setup aims to present a building that is 20 m long in the downwind direction, 30 m wide in the crosswind direction, and reaches a height (*H*) of 25 m. In the wind tunnel, this setup is approximated with elements that are about 200 times smaller, counting on the fact that similarity arguments at very large Reynolds numbers allow one to extrapolate the results to the target building size. The scaling factor of 200 is suggested by the CEDVAL and has been used by other models. In SAM, the building is represented on a Cartesian grid with a uniform grid-spacing of 1 m and domain size of 400 x 200 x 100 m in downwind (*x*), crosswind (*y*), and the vertical (*z*) directions, respectively. The horizontal dimensions of the domain closely reproduce the wind tunnel's dimensions multiplied by the scale factor of 200 while the domain top corresponds to only about half of the height of the actual wind tunnel. The reduced extent of the domain top, relative to the wind tunnel, was deemed acceptable as preliminary tests have shown that the flow barely changes at the height of the domain top. In the SAM simulation, the building center is located in the domain center at coordinates x = 0, y = 0 with its base at z = 0.

The horizontal inflow wind velocity used in the simulations is specified using a simple power-law profile $u(z) = U_{ref}(z/H_{ref})^{a}$, which is suggested by the CEDVAL and closely approximates the observed inlet profile. The factor a is set to 0.21 for both the A1-1 and A1-5 simulations. Then for A1-1 and A1-5, respectively, the reference height, H_{ref}, is set to 100 m and 125 m, and the reference windspeed,

U_{ref}, is set to 6.0 and 5.85 m/s. In both simulations, the inflow wind is aligned along the x direction. Since SAM uses a periodic domain in that direction, strong nudging of the wind profile is applied in the first 10% of the domain length (in the x direction) to maintain a close match to the specified inflow profile. Solid walls are placed at the four other sides of the domain to mimic the wind tunnel's walls. One caveat to mention is that the incoming flow in the CEDVAL experiments has been found to be somewhat turbulent with about a 20-30% turbulent intensity that is quite anisotropic, with horizontal turbulence having higher intensity than vertical turbulence. However, in our experiments we assume that the incoming flow is not turbulent as there is no clear way to initiate the required turbulence characteristics, which may have been caused by the particular construction of the wind-tunnel inlet. In terms of atmospheric stability, the temperature stratification is set to neutral to represent the wind-tunnel conditions.

The advection scheme used for all scalars is the fully three-dimensional monotonic and positive scheme MPDATA (Smolarkiewicz, 2006). The advection scheme for momentum is the second-order, centered-differences-in-flux form with conservation of kinetic energy. The surface everywhere is free-slip for simplicity, as at high Reynolds numbers (like in this case) the drag by the building surface does not have a large effect on the flow (it may affect the incoming profile near the surface, but we specify it). It might be important to use subgrid-scale (SGS) turbulent viscosity. However, for this case we tried both the Smagorinsky and 1.5-order closure for the SGS turbulence, based on prognostic SGS kinetic energy, and found little difference between the results.

To see the effect of additional iterations of the QSBM on the results and on the residual flow inside the building, three additional experiments were performed with one, two and three iterations. As will be discussed further, the number of iterations had small effect on overall results. Therefore, rather arbitrarily, most of the result will be presented using the simulation with two additional iterations.

Both simulations were run for 3900 s with a 0.05 s timestep. The first 900 steps are discarded as spin-up, so only the last 3000 s (i.e., 50-minutes) of each run are used for time averaging of the results. The averaging period is 750 times longer than characteristic time scale given by H/U_{ref} and, therefore, more than sufficient to obtain a statistically steady solution. Even though this may seem to be a very long integration, for the wind-tunnel model of the building, which is 200 times smaller, this simulation time would correspond to about 15 seconds in the wind tunnel. Also note that because SAM is a parallel and efficient model, each simulation took only about an hour on a supercomputer using 200 cores; therefore, by any measure, it cannot be considered a "computationally expensive" simulation.

b) Gas tracer release

The QSBM allows for small "leaks" of momentum and kinetic energy into the obstacles which may not be problematic for most applications but may become a problem for advection of conserved scalars. Thus, simulating the dispersion of gas tracer releases requires one additional code modification: setting the flux of scalars through the obstacles' boundaries to zero. In CEDVAL, the gas tracer is continuously released from four elongated openings at the bottom of the leeside wall of the building (representing four entrances to a parking garage) with a flow rate of 3 m/s; that is, they are not simple point sources. In SAM, these sources are simply modeled by four 3-grid-point continuous sources (i.e., 3 m) in the y direction right near the wall. Due to the constraint imposed on mass conservation in the incompressible model, it would be difficult to specify an additional flow of air, as in the actual gas tracer sources in CEDVAL. The absence of this additional flow may be responsible for some of the biases in the results. The CEDVAL dataset reports normalized gas tracer concentrations K, defined it as $K = C \times U_{ref} \times H^2/Q_s$, where C is actual concentration and Q_s is total specified gas tracer release rate. This normalization process eliminates the need to produce a precise match between observed and simulated release rates such that an arbitrary release rate can be used in the model.

c) Time-average flow

The A1-1 dataset contains wind measurements for two planes, vertical at y/H=0 (i.e., vertically through the center of the building) and horizontal at z/H=0.28 (i.e., horizontally at 7 m above the base of the building). We begin by performing a qualitative evaluation of the main flow features in the planes as a whole, and then we offer a more qualitative evaluation in specific columns of the model.

Beginning with the vertical plane, Figure 1 illustrates the 50-min averaged flow streamlines (combined u, w components) color coded by the wind speed in the wind tunnel (top panel) and in the simulation (bottom panel). Overall, the simulation captures well the main observed features of the flow around the building in this plane. In front of the building below the rooftop level, the flow separates into the so-called horseshoe vortex, where below ~2/3 of the building height the flow dives towards the surface while above that height the flow rides upward and over the building rooftop. Both the observations and model show a rotation vortex upwind of the building face near the surface. That said, we note that the rotation center of the simulated vortex is farther away from the building than in observations. Over the rooftop of the building, a "separation bubble" develops, which is well reproduced by the model. In the building's wake, a large leeside vortex is present, which, on this x-z cross-section, is a visible part of a so-called "arch vortex" developing behind the building. The flow reverses direction in the low part of the leeside vortex, resulting in converging flow towards the building and rising flow along the leeside wall towards the rooftop. The position of the center of rotation of the leeside vortex is captured by the model quite well, albeit the simulated position is a bit higher than observed. Also, the simulated vortex extends as far as x/H = 1.9 (47 m) in the simulation compared to x/H = 1.7 (42 m) in the observations. We note that other models also have tended to overextend the leeside vortex in this CEDVAL case (e.g., Gorlé et al., 2010; Trini Castelli & Reisin, 2010; Parente et al., 2011; Zhang et al., 2016).

Table 1 summarizes the comparison with the CEDVAL observations for the whole $y/H=0$ plane as well as for three key zones shown in Figure 1, the windward zone (W), leeside zone (L), and the zone above the rooftop (R). Here we follow the methodology by Zhang et al. (2016). The mean relative error (*RE)* of the wind velocity for the whole plane is 2.0% with an *RMSE* of 0.42 m/s; the overall spatial correlation with observations R = 0.97. As expected, the biggest challenge for the model is the leeside flow, where the *RE* is the largest, 18.6%, and *R* = 0.91. The windward *RE* is rather small, 1.6% but, because of the error in the center position of the horseshoe vortex, the correlation is only 0.87. The flow over the rooftop is simulated the best, with *RE* = 0.7% and *R*=0.98.

Moving on to the horizontal plane, Figure 2 illustrates the 50-min averaged flow streamlines (combined *u*, *v* components) color coded by the wind speed in the wind tunnel (top panel) and in the simulation (bottom panel). Again, the main characteristics of the flow in that plane are well reproduced by the model. Those include the "separation bubbles" at the building's sides that consist of two counterrotating vortices and the position of rotation centers at the leeside of the building. This pair of vortices at the leeside is also a part of the arch vortex. The acceleration of the flow around the building corners is well reproduced not only qualitatively, but also quantitatively.

Table 2 summarizes the statistics of the flow for the whole *z/H*=0.28 plane as well as separately for three key zones shown in Figure 2, the windward zone (W), the zone across the lateral walls (S), and leeside zone (L). For the whole plane, *RE* = 9.4% and *R*=0.91. The largest *RE* = 16.1% is found in the front of the building with *R*=0.93. The overall leeside flow is reproduced better, with *RE*= 10.2% and *R*=0.92. Despite the fact that the model performs better in the zone across the lateral walls in terms of the mean wind with *RE* = 7.1%, the spatial correlation of the wind velocity is only *R* = 0.86. Overall, our statistical results summarized by Tables 1 and 2 are quite close to the results presented by Zhang et al. (2016).

Figures 3 and 4 offer another way of evaluating the simulated flow in the same planes as the previous figures. In addition, these figures present results obtained for using different number of iterations of the QSBM whereas Figures 1 and 2 only show results using 2 iterations.

Beginning with the vertical plane, Figure 3 shows vertical profiles of the 50-min mean horizonal (along the *x* axis; *u*) and vertical (*w*) velocities at various distances from the building center along the x axis at *y/H* = 0 (i.e., along the direction of the wind passing through the center of windward and leeward building faces). As mentioned above, the main inconsistency with the observations is that the horseshoe vortex near the surface is relatively farther upstream from the building, as evident by the velocity profiles at x/H = -1. Closer to the windward wall (x/H = -0.6), the magnitude of both downward and upward vertical velocities and the position of the stagnation point (w = 0) are reproduced quite well, although w near the rooftop level is overestimated by about 1 m/s. Both profiles above the rooftop at the building's center (x/H=0) are reproduced very well. The profiles through the leeside vortex (x/H = 0.6 and x/H = 1) also show good agreement with the observations. One can clearly see the reverse return flow towards the building throughout most of the building height. The profile of the mean wind in the building's wake at x/H = 3, which is relatively far away from the flow reconnection point, is also well reproduced.

Moving on to the horizontal plane, Figure 4 shows horizontal profiles of u and v at various distances from the building center along the x axis at z/H = 0.28. Overall, the profiles are reproduced quite well by the model. There is a slight underestimation of the incoming velocity in front of the building at x/H=-0.6. Also, there are two "kinks" in the corresponding v profile in front of the building corners at the distance of ±0.7 from the center line, which can be explained by some noise generated by the second-order advection scheme for momentum because of the sharp corners of the building. The acceleration of the flow and the flow towards the building near its side walls at x/H=0 is in good agreement with observations. In the leeside, at x/H=0.6 and x/H=1.0, the magnitude of the return flow towards the building is reproduced very well, although the downwind velocity outside of the return flow is clearly underestimated. The profiles of the reconnected flow at x/H=3.0 is also well reproduced.

d) Residual flow inside the building

The results shown in Figures 3 and 4 indicate that the number of iterations used in the QSBM have only a minor impact on the mean flow. For completeness, we explore their impact on the residual flow inside the building. Figure 5 shows the 50-min mean horizonal (along the x axis; u) and vertical (w) velocities or "residual velocities" in the vertical plane y/H = 0 (i.e., along the direction of the wind passing through the center of windward and leeward building faces) for simulations relying on various numbers of iterations in the QSBM. When no iterations are performed, the maximum residual velocity inside the building is about 0.1 m/s at the upper inflow corner. The largest standard deviation of the residual velocity is smaller than 0.005 m/s (not shown). Considering that the inflow wind is several meters-per-second, it is fair to say these residual velocities are already quite small. Each iteration further reduces the residual velocity by about a factor of two; so after two and three iterations, the maximum residual velocities in the plane decrease to about 0.02 and 0.01 m/s, respectively. In terms of computational expense, the bi-directional-FFT pressure solver takes about 20% of running time in the particular parallel model configuration running on 200 CPUs, so each additional iteration adds about 20% to the expense.

e) Turbulence

So far, we have presented time averaged results. It is also important to see the ability of the model to simulate the turbulence associated with the flow around a building. As was mentioned above, the incoming flow in the simulation is not turbulent, but the incoming flow in the wind-tunnel experiment already has some turbulence, especially in the *u*-component. There is no simple way to initialize the anisotropic turbulence in the model to mimic the turbulence at the inlet of the wind tunnel. The turbulent kinetic energy of the incoming flow would contribute some additional turbulence behind the building, and this factor is absent in the simulation. However, most of turbulence is generated by the building itself; therefore, with the aforementioned caveat in mind, we will still compare the turbulent intensities produced by the model against the observations.

Figure 6 compares the turbulent intensity, or the standard deviation of turbulent wind velocity fluctuations, individually for each of the wind components in the vertical symmetry plane $y/H = 0$. Unfortunately, only turbulent intensities for the u and w components of the wind are reported in that plane by the CEDVAL A1-1 dataset. The region with maximum turbulence is just above the building rooftop in both the simulations and observations. On the leeside, the turbulence is relatively weak immediately behind the building within the distance approximately equal to the building's height, as in observations. The highest levels of turbulent intensity of the u component are generally above the building's rooftop height as observed. On the contrary, the maximum intensity of the *w*-component is generally below the rooftop height mostly above the upper half of the building. Overall, the spatial structure of the turbulent regions behind in the wake of the building is well reproduced by the model.

f) Gas tracer transport

Figure 7 shows normalized gas tracer concentration in the vertical plane at y/H=0. The greatest concentrations are found near the ground close to the leeside wall, where the sources are. In the simulation, the gas tracer concentration reaches a maximum of 56.3 normalized units vs the 66.7 normalized units in the wind tunnel. The gas tracer is transported by the leeside vortex up along the leeward wall towards the rooftop, where it gets swept into the "separation bubble" above the rooftop. Overall, the model seems to reproduce the observed distribution of concentration rather well, especially throughout the leeside vortex, but tends to underestimate concentration above the rooftop.

Figure 8 shows normalized gas tracer concentration in horizonal planes at z/H = 0.08 (2 m) and z/H = 0.28 (7 m). Overall, the horizontal distribution of gas tracer concentration at the leeside is reproduced quite satisfactory in both horizontal planes. The main model biases are within the "separation bubbles" along the side walls of the building, like the one over the rooftop, where concentration is also underestimated. Nevertheless, the gas tracer seems to penetrate all the way to the front corners of the building, like in observations. The apparent difficulty that the model has with the cavities along the side walls and over the rooftop can be attributed to the flow being rather unresolved there, as the thickness of the "bubbles" (see Figures 1 and 2) are only several grid cells. Also, as mentioned before, the sources of gas tracers in the wind-tunnel experiment are not point sources but, rather, are jets ejecting gas tracer with the speed of 3 m/s from four elongated openings in the leeward building's wall. It is not clear how to mimic such dynamic sources of gas tracers in SAM.

4. Simulations of obstacles not aligned with the grid

In the previous section, we reported the results of flow around an idealized rectangular building when the boundaries are perfectly aligned with the grid cells' boundaries which, arguably, is an ideal situation for testing our method. However, an important question remains as to how universal the proposed method is when applied to obstacles with boundaries that are not aligned with the numerical grid. To answer this question, we apply the QSBM method to two other cases. In the first case, we simulate the flow around a building in a shape of a cube rotated 45^o relative to the flow and also to the grid; i.e., with its corner facing the incoming flow. In the second case, we consider flow around a building in the form of a circular cylinder with a height/diameter ratio of one. In each case, an obstacle is represented by a population of whole grid cells that fit inside its actual geometric boundaries.

a) A cubic building rotated 45^o

This test is based on the CEDVAL A1-6 case of a cube rotated 45^o relative to the direction of the incoming flow. In the dataset, the size scaling factor of 200 is also suggested, so the cubic building has H=25 m size for all dimensions. The incoming flow profile is the same as in A1-1 case. The model grid and duration of the run are also identical to our simulation of the A1-1 case. Figure 9 compares model to observations, showing the wind vectors at the y/H=0 symmetry plane and horizontal cross-section at the z/H=0.4 height. Note that, unlike the A1-1 case, the measurements of the wind in A1-6 case were relatively sparse. In the figure, all the available data are plotted, with model results shown at the same locations as the measurements. One can see that in the case of rotated cube, there is a clear horse-shoe vortex does not develop upstream from the building as was the case in A1-1. There is also virtually no acceleration of the flow above the building and no indication of the separation bubble developing over the roof. The bulk of the flow seems to prefer to go around the building's side corners rather over the top of the building. The model seems to capture this behavior rather well, both qualitatively and quantitatively. In the leeside of the building, the arch-vortex also develops, with a leeside vortex and associated reverse flow towards the building clearly visible in the vertical cross-section. The leeside extent of the flow seems to be somewhat overestimated in the simulation, as in the A1-1 case, but it is difficult to quantify that difference due to the sparsity of observations. Similar to the A1-1 case, there is a pair of vortices behind the building (only one of them is actually shown), clearly visible in the horizontal cross-section. The model seems to shift the center of rotation further downstream than in observations, probably because of the rather rough representation of the building walls in this case when the grid is not aligned with the building surfaces.

Tables 3 and 4 present statistics of comparisons with the CEDVAL observations for *y/H=0* and z/H=0.4 planes, respectively, for windward zone (W) and leeside zone (L) shown in Fig. 9 as well as for all observations for a given plane. For the vertical *y/H=0* plane, the *RE* of the wind velocity is 7.6% with an *RMSE* of 0.42 m/s and *R* = 0.96. The biggest challenge for the model is before is the leeside flow, where the *RE* is the largest, 9.3%, and *R* = 0.94. The windward *RE* is also relatively large, 6.2%, but the correlation is very high 0.99. The flow over the rooftop is simulated the best, with *RE* = 0.7% and *R*=0.98. For the horizontal *z/H*=0.28 plane as the whole, *RE* = 6.1% and *R*=0.91. The largest *RE* = 13.5% is found again in the leeside zone with *R*=0.89, while the windward zone is simulated much better with *RE* = 4.2% and R=0.94. Overall, we may conclude that the flow in this case of rotated cubic building is simulated reasonably well.

b) A flow around a circular cylinder

To further investigate the ability of our method to simulate the flow around obstacles that have boundaries not aligned with the Cartesian grid, we simulate the flow around a circular cylindrical building with the aspect ratio (ratio of height to diameter) of one. We use the setup from an LES study by Kumar and Tiwari (2021; further KT21), which, in turn, is based on the experimental and LES results reported by Pattenden et al (2007; further P07). The latter used a structured grid conformal to the cylinder shape, while the former used the conventional IBM on a Cartesian grid. In KT21, the incoming wind profile was obtained first by a separate LES simulation of a neutral surface layer over a flat surface with a given roughness length z_o. It was found that the resultant profile is very close to a log-law profile

$u(z) = \frac{u_*}{k} ln \frac{z}{z_o}$, where u_*=0.29 m/s, z_o=0.046 m, and k is von Karman constant. In KT21, the height of the cylinder is 4 m. We scaled up the size of the cylinder by a factor of 10 to *H*=40 m, which would be a more reasonable size for a building. To maintain the self-similarity of the flow, a factor of 10 increase was also applied to the roughness length in the specified log-law wind profile, yielding z_o= 0.46 m. The grid spacing was also increased to 1 m from the 0.1 m in KT21, to preserve the relative grid resolution of the cylinder. The numerical domain is chosen to be the same in the horizontal directions as in the previous runs, but the domain is twice as tall because the building is also taller than before. The time step and run duration were the same as in the previous runs.

Figure 10 illustrates the overall structure of the time-averaged flow around the cylinder showing velocity vectors in the vertical plane through the center of the cylinder as well as in the horizontal plane at cylinder's mid-height. Overall, all the features that we saw in the case of rectangular building are present, namely: a horse-shoe vortex in front of the cylinder, an arch-vortex in the leeside with the return flow towards the cylinder in its wake with a pair of counterrotating vortexes, and the separation "bubble" over its top. The flow features are consistent with the results presented by KT21 (see their Figs 5 and 6). However, there are some clear differences. Similar to the simulation of the rectangular building, the horse-shoe vortex is overextended upstream with the position of separation point near the surface at *x/H* = -2 compared to the observed *x/H* = -1 given in P07. This is probably due to our use of free-slip conditions and insufficient vertical resolution near the surface. Note that the position of the separation point is also overextended in KT21 (*x/H* = -1.5) and LES results by P07 (*x/H* = -1.45). The height of the stagnation point, where the separation of the incoming flow into upward and downward branches occurs at the upstream surface of the cylinder, is at *z/H* = 0.7, which is close to *z/H* = 0.65 reported by KT21. The surface position of the flow reattachment point of the leeside vortex is also overextended at about *x/H* = 2.2, compared to the observed *x/H* = 1.6. However, the KT21 and P07 studies also had difficulty reproducing this parameter, reporting *x/H* = 1.95 and *x/H* = 2.1, respectively. On the top of the cylinder, the reattachment of the separated flow is at *x/H* = 0.35, same as in KT21 and close to *x/H* = 0.39 in P07.

It is rather common when modeling the flow around blunt objects, such as a cylinder, to look at a so-called pressure coefficient: $C_p = (p - p_\infty)/\frac{1}{2}\rho V_\infty$, where p is the pressure on the object's surface, ρ is air density, p_∞ and V_∞ are the pressure and velocity upstream of the flow far from the object. In the case of a cylinder, the pressure coefficient is measured along its surface at some fixed height as a function of the angle Φ in cylindrical coordinates relative to the cylinder's center, usually between $\Phi = 0^{\circ}$ and $\Phi = 180^{\circ}$ which is between upstream and downstream points of the cylinder's surface. Figure 11 compares C_p at *z/H* = 0.5 to the modeling and experimental results presented by P07 superimposing our results on their Fig. 7. One can see that overall, the distribution of pressure coefficient near the cylinder's surface is captured rather well by SAM. Some apparent noisiness of the SAM results is associated with the rather rough approximation of the curved cylinder surface by rectangular cells in our method. We can also use the pressure coefficient to compute the drag coefficient C_D, which, in case of a cylinder, is computed as $C_D = \int_0^{\pi} C_p cos\,\Phi d\Phi$ (e.g., Bertin 2002). From our results, we obtain the drag coefficient to be 0.82, which is close to the observed value of 0.79 reported by P07.

5. Summary

In this paper, we present a method for incorporating obstacles, such as buildings, into SAM. This model is usually used to address climate-related questions but can be also employed as an LES model to answer emerging urban microclimate questions. The method, which we call the Quasi-Solid Box Method (QSBM), can be considered to be a subset of the immersed-boundary method (IBM), called the force-body methods, that stagnate the flow everywhere inside an obstacle. Unlike some other force-body methods that use fictitious damping or relaxation terms in the momentum equations, the QSBM avoids them by explicitly setting the provisional velocity components to zero in the cells that are inside an obstacle, right before applying the pressure-gradient terms to enforce non-divergence of the flow.

We tested the method using a case of a flow past an idealized single rectangular building in neutral atmospheric conditions and compared the results to the CEDVAL wind-tunnel observations. Overall, the model performance in this case can be considered satisfactory. All major flow features are well reproduced, such as the existence of an arch vortex in lee of the building, the horseshoe vortex and the height of the separation point of the inflow in front of the building, and the "separation bubbles" over the rooftop and on building sides. The model has a difficulty, though, reproducing the exact position of the center of rotation of the horseshoe vortex and tends to overestimate slightly the extent of the leeside vortex. On the other hand, the vertical wind structure of the flow above the rooftop and downstream from it is reproduced quite well, particularly the strength of the return flow towards the leeside wall. The highest levels of turbulence are simulated above the building rooftop, in accord with observations. A relatively calm zone, with relatively low levels of turbulence, is found behind the building within the distance approximately equal to the building's height, also as in observations.

The QSBM allows a residual flow inside the obstacles that is very small compared to the magnitude of velocity in its vicinity; however, the residual velocities can be further reduced by iterating over the last steps that enforce zero velocity and non-divergence of the flow. The added expense is about 20% increase of running time per each additional iteration. In this study, each additional iteration would reduce the maximum magnitude of residual velocities inside the building by about a factor of two. However, overall, the use of iterations makes only a minor improvement over the simulation with no iterations. This conclusion might not be generalizable, so, ideally, sensitivity of the results to at least a single iteration should be tested when the method is employed to simulate other cases.

We additionally evaluate the ability of this method to handle the dispersion of gas tracers. The gas tracer dispersion also agrees rather well with observations, although some challenges remain in reproducing transport of gas tracer into the "separation bubbles", not only over the rooftop, but also along its crosswind sides.

One of the drawbacks of the QSBM is that it requires approximation of any obstacle as a collection of whole grid cells that fit inside the obstacle's actual geometric boundaries. This was not a problem in our simulation of a rectangular building as, in this case, the grid-cell boundaries conform to the building's boundaries perfectly. However, in the case of a city, simulated buildings may not conform to the grid-cell boundaries; so, as a result, they may have staircase-like walls. To evaluate the performance of the method in such cases, we presented the results of two additional simulations. The first is based on another CEDVAL case of the flow around a cubic building rotated by 45^{o} to the direction of the incoming flow; the second case is for a cylindrical building with the aspect ratio of one, obtained from a different observational dataset and to which our results are compared to published results from two other LES models. Overall, the rotated building results compare rather well to the wind tunnel observations, both qualitatively and quantitatively. The biggest bias was in the exact position of the arch-vortex and some overextension of the leeside-vortex. In the case of the flow around the cylindrical building, all major observed features of such a flow have been fairly well represented by the model. Some notable biases are found, such as the position of a horse-shoe vortex and the extent of the leeside vortex. However, these biases are generally similar to those shown by other LES models for this case, which can be the indication of some fundamental difficulties in simulating such obstacles that are not necessarily SAM-specific. Despite the biases in the position of vortexes, the angular distribution of a pressure coefficient around the cylinder and closely related aerodynamic drag coefficient have been well simulated by SAM when compared to actual measurements.

Overall, we find the results of the tests reported in this study to be quite encouraging. However, we caution that the QSMB should not be viewed as computationally inexpensive alternative to a more comprehensive and accurate traditional IBM. We implemented this method in SAM primarily to be able to simulate the turbulence and tracer transport around a city in the planetary boundary layer, when the buildings are relatively coarsely represented due to the computational cost. For such problems, the QSBM becomes a very attractive approach as its implementation requires very minor code modifications without affecting the computational efficiency of SAM.

Acknowledgements. This work was supported by the Brookhaven National Laboratory under its Laboratory Directed Research and Development (LDRD) Program, Project #20-002. This research used resources of the National Energy Research Scientific Computing Center; a DOE Office of Science User Facility supported by the Office of Science of the U.S. Department of Energy under Contract No. DE-

AC02-05CH11231. All model output used in this study is accessible through NCAR Campaign Storage via Globus.

References

Bertin J.J. (2002). Aerodynamics for Engineers, 4th edition, Prentice Hall.

Blocken, B. (2018). LES over RANS in building simulation for outdoor and indoor applications: A foregone conclusion? *Building Simulation*,11(5), 821–870.

Chan, S. T., & Leach, M. J. (2007). A validation of FEM3MP with Joint Urban 2003 data. *J. Appl. Meteor. and Clim.*, *12*, 2127–2146.

Diehl, S.R., Burrows, D.A., Hendricks, E.A., & Keith, R. (2007). Urban dispersion modeling: Comparison with single-building measurements. *J. Appl. Meteor. Climatol.*, **46,** 2180–2191.

Duran, D. R. (1991). The Third-Order Adams-Bashforth Method: An Attractive Alternative to Leapfrog Time Differencing. *Mon. Wea. Rev*, 119(3), 702-720.

Fortunato, A. B., and A. M. Baptista, 1996: Evaluation of horizontal gradiaents om sigma coordinate shallow water models. *Atmos. Ocean* 34, 489-514.

Gal-Chen, T., & Somerville, C.J. (1975). On the use of a coordinate transformation for the solution of the Navier–Stokes equations. *J. Comput. Phys*., 17, 209–228.

Gorlé, C., van Beeck, J., & Rambaud, P. (2010). Dispersion in the Wake of a Rectangular Building: Validation of Two Reynolds-Averaged Navier–Stokes Modelling Approaches. *Boundary-Layer Meteorol,* **137,** 115–133. https://doi.org/10.1007/s10546-010-9521-0

Hanna, S., and Coauthors, 2006: Detailed simulations of atmospheric flow and dispersion in downtown Manhattan: An application of five computational fluid dynamics models. *Bull. Amer. Meteor. So*c., 87, 1713–1726.

Iaccarino, G., and R. Verzicco, (2003). Immersed boundary technique for turbulent flow simulations. *Appl. Mech. Rev*., 56, 331–347.

Khairoutdinov, M. F., & Randall, D.A. (2003). Cloud-resolving modeling of the ARM summer 1997 IOP: Model formulation, results, uncertainties, and sensitivities. *J. Atmos. Sci*., 60, 607-625.

Korycki, M; Lobocki, L, and Wyszogrodzki, A, 2016: Numerical simulation of stratified flow around a tall building of a complex shape. *Environ. Fluid Mech*, 16(6), 1143-1171.

Kumar P. and Tiwari, S. (2021): Effects of size ratio and inter-cylinder spacing on wake transition in flow past finite inline circular cylinders mounted on plane surface, *Physics of Flui*ds, 33, 023602 https://doi.org/10.1063/5.0037712

Lundquist, K. A., F. K. Chow, and J. K. Lundquist (2010): An immersed boundary method for the Weather Research and Forecasting Model. *Mon. Wea. Rev*., 138, 796–817, https://doi.org/10.1175/2009MWR2990.1.

Lundquist K.A., Chow F.K., Lundquist J.K. (2012) An immersed boundary method enabling large-eddy simulations of flow over complex terrain in the WRF model. *Mon Wea Rev* 140, 3936–3955. https://doi.org/10.1175/MWR-D-11-00311.1

Muñoz-Esparza, D., Sauer, J. A., Shin, H. H., Sharman, R., Kosović, B., Meech, S., et al. (2020). Inclusion of building-resolving capabilities into the FastEddy® GPU-LES model using an immersed body force method. *J. of Adv. in Model. Earth Sys.*, *12*, e2020MS002141. https://doi.org/10.1029/2020MS002141

Mittal, R., & Iaccarino, G. (2005). Immersed Boundary Methods. *Ann. Rev. of Fluid Mech*., 37, 239–261.

Parente, A., Gorlé, C., van Beeck, J., & Benocci, C. (2011). Improved k-e model and wall function formulation for the RANS simulation of ABL flows. *Journal of Wind Engineering and Industrial Aerodynamics*, **99**, 267–278.

Pattenden, R. J., N. W. Bressloff, S. R. Turnock, and X. Zhang, (2007): Unsteady simulations of the flow around a short surface-mounted cylinder. *Int. J. Numer. Methods Fluids*, 53, 895–914.

Profiroiu, C. M., Bodislav, D. A., Burlacu, S., & Rădulescu, C. V. (2020). Challenges of Sustainable Urban Development in the Context of Population Growth. *European Journal of Sustainable Development*, 9, 3, 51-57. doi: 10.14207/ejsd.2020.v9n3p51

Smolarkiewicz, P.K. (2006). Multidimensional positive definite advection transport algorithm: an overview. *Int. J. Numer. Methods Fluids*, 50, 1123–1144.

Smolarkiewicz, P. K., Sharman, R., Weil, J., Perry, S. G., Heist, D., & Bowker, G. (2007). Building resolving large-eddy simulations and comparison with wind tunnel experiments. *Journal of Computational Physics*, *227*(1), 633–653.

Trini Castelli, S., & Reisin, T.G. (2010). Evaluation of the atmospheric RAMS model in an obstacle resolving configuration. *Environ Fluid Mech.,* **10,** 555–576. https://doi.org/10.1007/s10652-010-9167-y

Zhang, N., Du, Y., & Miao, S. (2016). A microscale model for air pollutant dispersion simulation in urban areas: Presentation of the model and performance over a single building. *Adv. Atmos. Sci.,* **33,** 184–192. https://doi.org/10.1007/s00376-015-5152-1

Zhang, N., and Z.C. Zheng (2007): An improved direct-forcing immersed-boundary method for finite difference application. *J. Comp. Phys*., 221, 2250-268.

Tables

Table 1 Comparison of CEDVAL A1-1 observations and simulation for the whole plane *y/H*=0 and for zones shown in Figure 1 for mean (*MN)*, absolute error ($E = MN_{sim}-MN_{obs}$), relative error ($RE=|E/MN_{obs}|$), root-mean-square error (RMSE), and correlation coefficient (*R*).

Zone	MN_{obs}(m/s)	MN_{sim}(m/s)	*E* (m/s)	*RE*	*RMSE* (m/s)	*R*
W - Windward	2.59	2.63	0.04	1.6%	0.60	0.87
L - Leeside	1.41	1.14	-0.26	18.7%	0.47	0.91
R – Rooftop	4.58	4.61	0.03	0.7%	0.29	0.98
y/H=0	3.28	3.22	-0.06	2.0%	0.42	0.97

Table 2 Comparison of CEDVAL A1-1 observations and simulation for the whole plane *z/H*=0.28 and for the zones shown in Figure 2 for mean (*MN)*, absolute error ($E = MN_{sim}-MN_{obs}$), relative error ($RE=|E/MN_{obs}|$), root-mean-square error (RMSE), and correlation coefficient (*R*).

Zone	MN_{obs}(m/s)	MN_{sim}(m/s)	*E* (m/s)	*RE*	*RMSE* (m/s)	*R*
W - Windward	2.51	2.11	-0.40	16.1%	0.50	0.93
L - Leeside	2.48	2.23	-0.25	10.2%	0.53	0.92
S – Sides	3.42	3.18	-0.24	7.1%	0.79	0.86
z/H=0.28	2.81	2.55	-0.26	9.4%	0.55	0.91

Table 3 Comparison of CEDVAL A1-6 observations and simulation for the whole plane *y/H*=0 and for the zones shown in Figure 9 for mean (*MN)*, absolute error ($E = MN_{sim}-MN_{obs}$), relative error ($RE=|E/MN_{obs}|$), root-mean-square error (RMSE), and correlation coefficient (*R*).

Zone	MN_{obs}(m/s)	MN_{sim}(m/s)	*E* (m/s)	*RE*	*RMSE* (m/s)	*R*
W - Windward	3.23	3.43	0.2	6.2%	0.23	0.99
L - Leeside	2.98	3.25	0.27	9.3%	0.55	0.94
y/H=0	3.21	3.45	0.24	7.6%	0.42	0.96

Table 4 Comparison of CEDVAL A1-6 observations and simulation for the whole plane *z/H*=0.4 and for the zones shown in Figure 9 for mean (*MN)*, absolute error ($E = MN_{sim}-MN_{obs}$), relative error ($RE=|E/MN_{obs}|$), root-mean-square error (RMSE), and correlation coefficient (*R*).

Zone	MN_{obs}(m/s)	MN_{sim}(m/s)	*E* (m/s)	*RE*	*RMSE* (m/s)	*R*
W - Windward	2.42	2.52	0.1	4.2%	0.23	0.94
L - Leeside	1.81	1.56	-0.24	13.5%	0.57	0.89
z/H=0.4	2.08	1.95	-0.13	6.1%	0.44	0.91

Figures

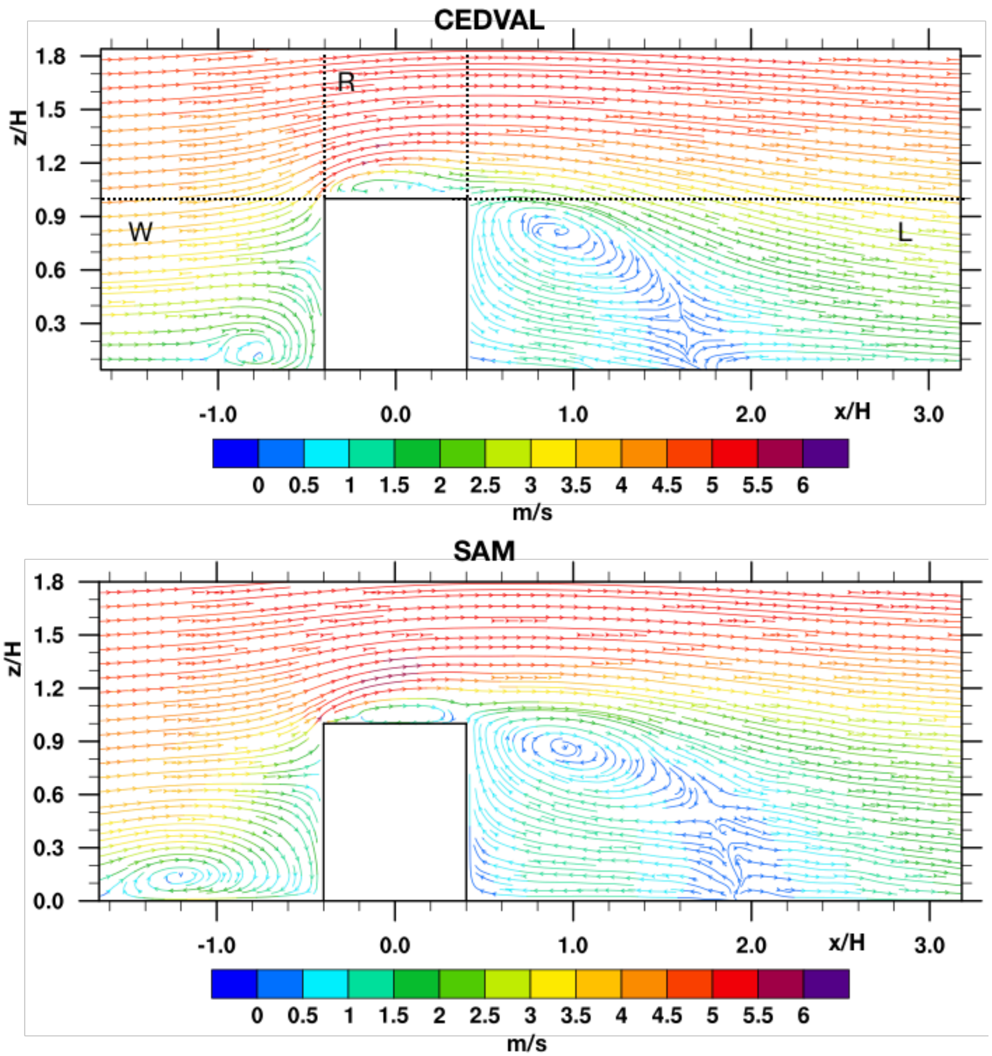

Figure 1. Vertical cross-section of wind at $y/H = 0$ for CEDVAL observations (top) and SAM simulation (bottom). The coordinates are normalized by height of the building. The dashed lines in the top plot indicate the boundaries of the key zones used for statistical comparison: W – windward in front of the building; R – above the rooftop; L – leeside vortex and wake zone.

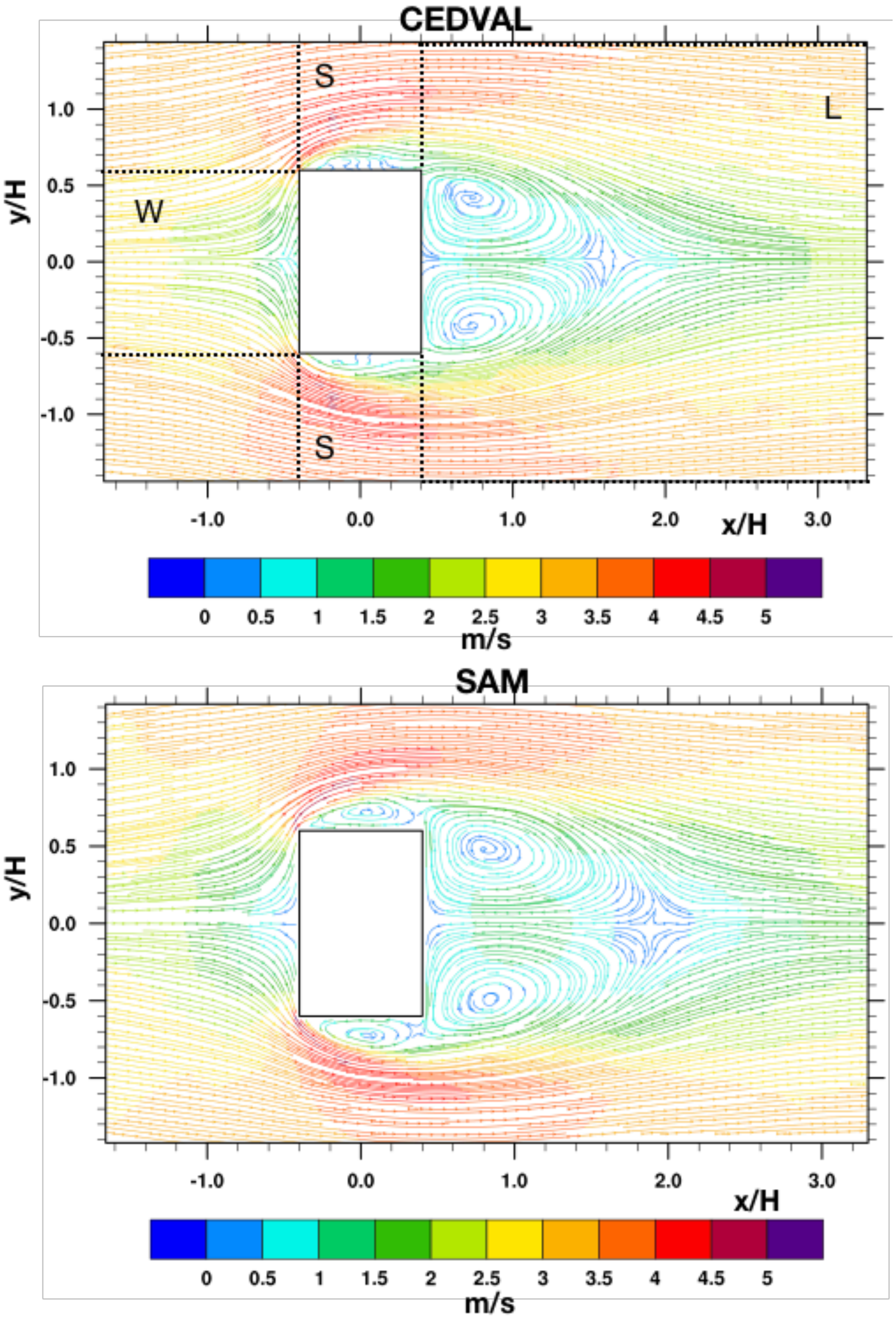

Figure 2. Horizontal cross-section of wind at *z/H* = 0.28 for CEDVAL observations (top) and SAM simulation (bottom). The coordinates are normalized by height of the building. The dashed lines in the top plot indicate the boundaries of the key zones used for statistical compasrison: W – windward in from of the building; S – across from lateral side walls; L – leeside vortices and wake zone.

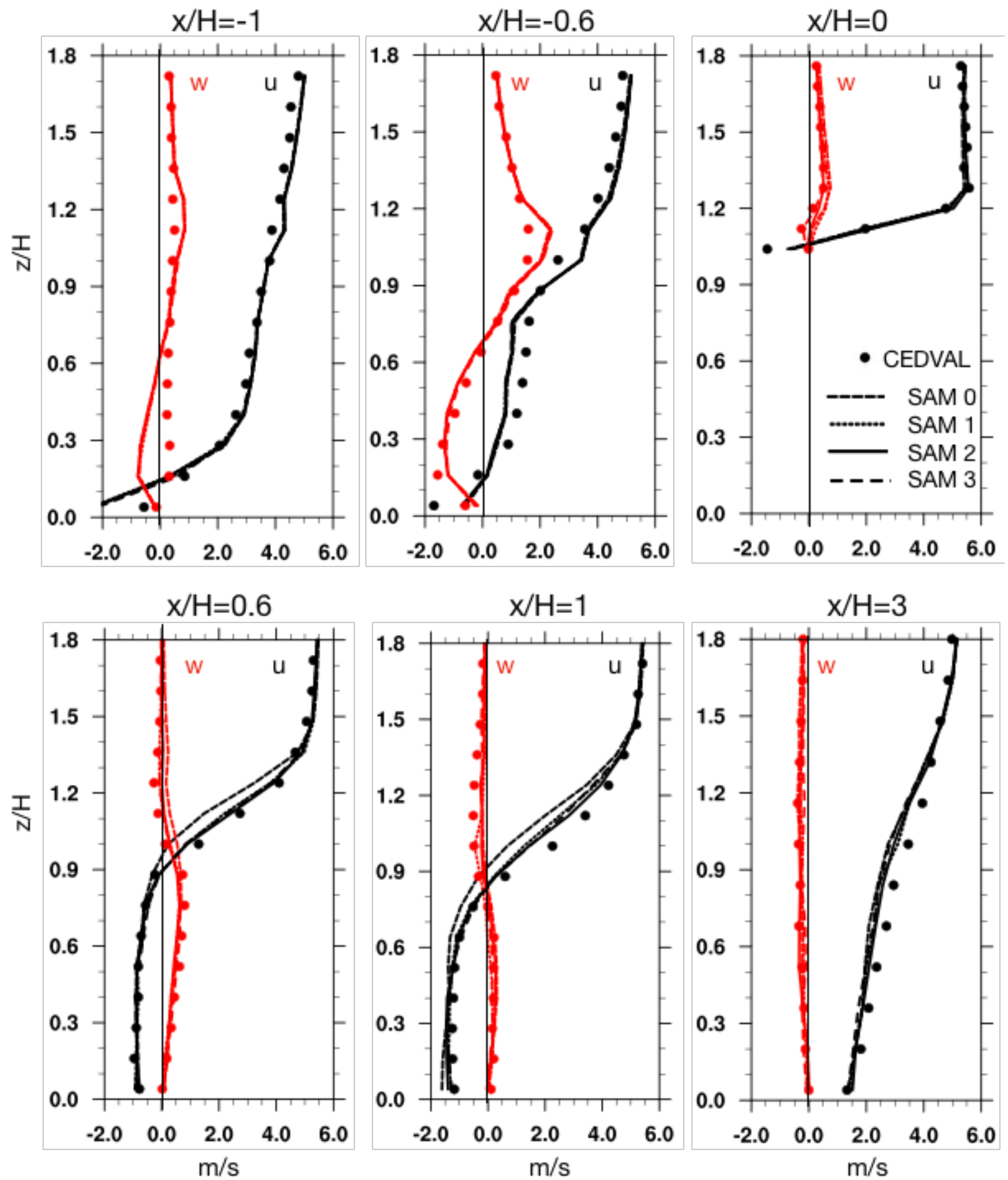

Figure 3. Vertical profiles of wind components at y/H=0. The results from SAM are shown by the lines for different number of iterations, from 0 to 3, as indicated in the top-right panel legend. Circles present the CEDVAL data; black and red colors represent the horizontal (u) and vertical (w) wind components, respectively.

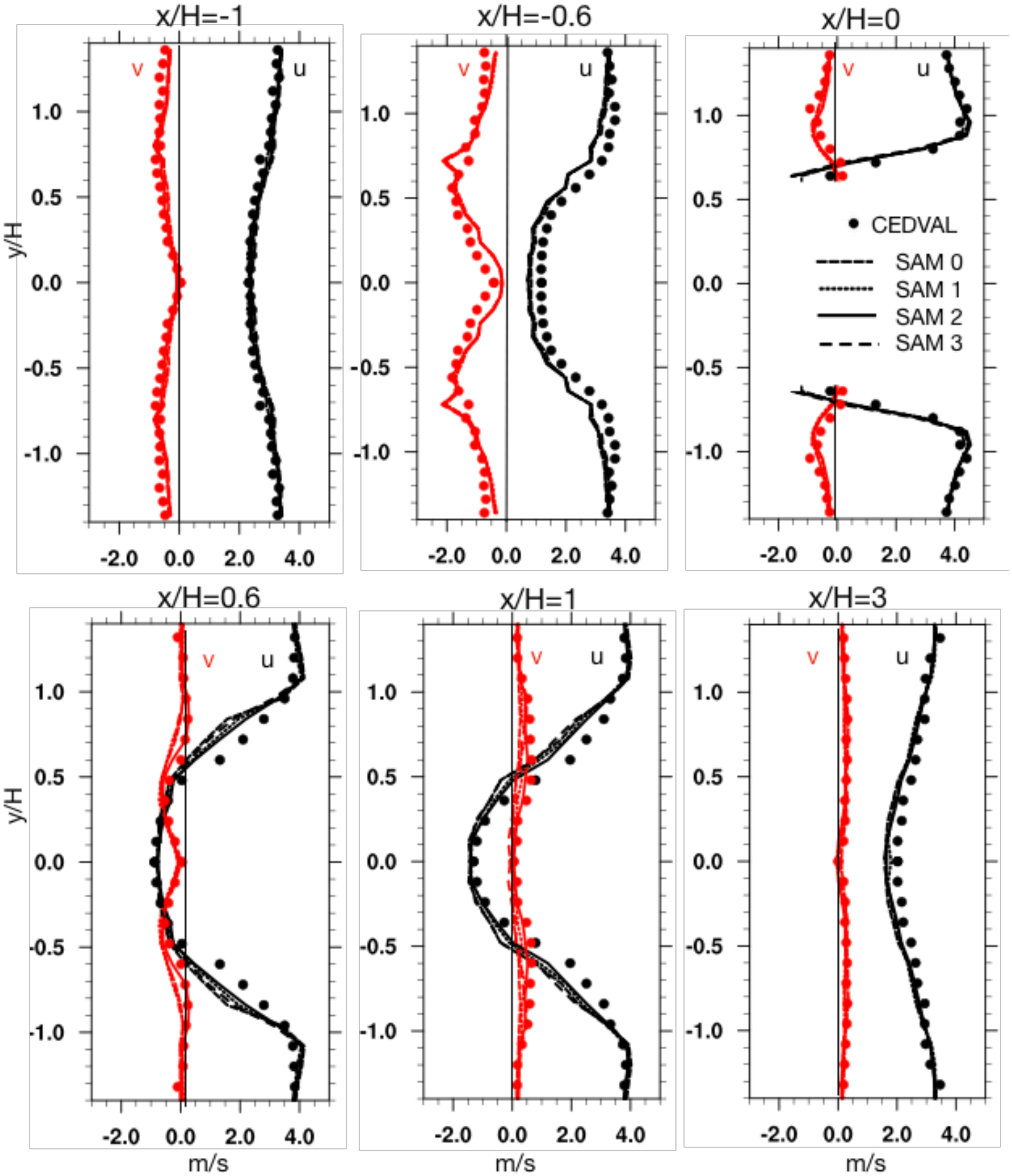

Figure 4. Horizontal profiles of wind components at z/H=0.28. The results from SAM are shown by the lines for different number of iterations, from 0 to 3, as indicated in the top-right panel legend. Circles present the CEDVAL data; black and red colors represent the horizontal wind components of (u) and (w) wind components, respectively.

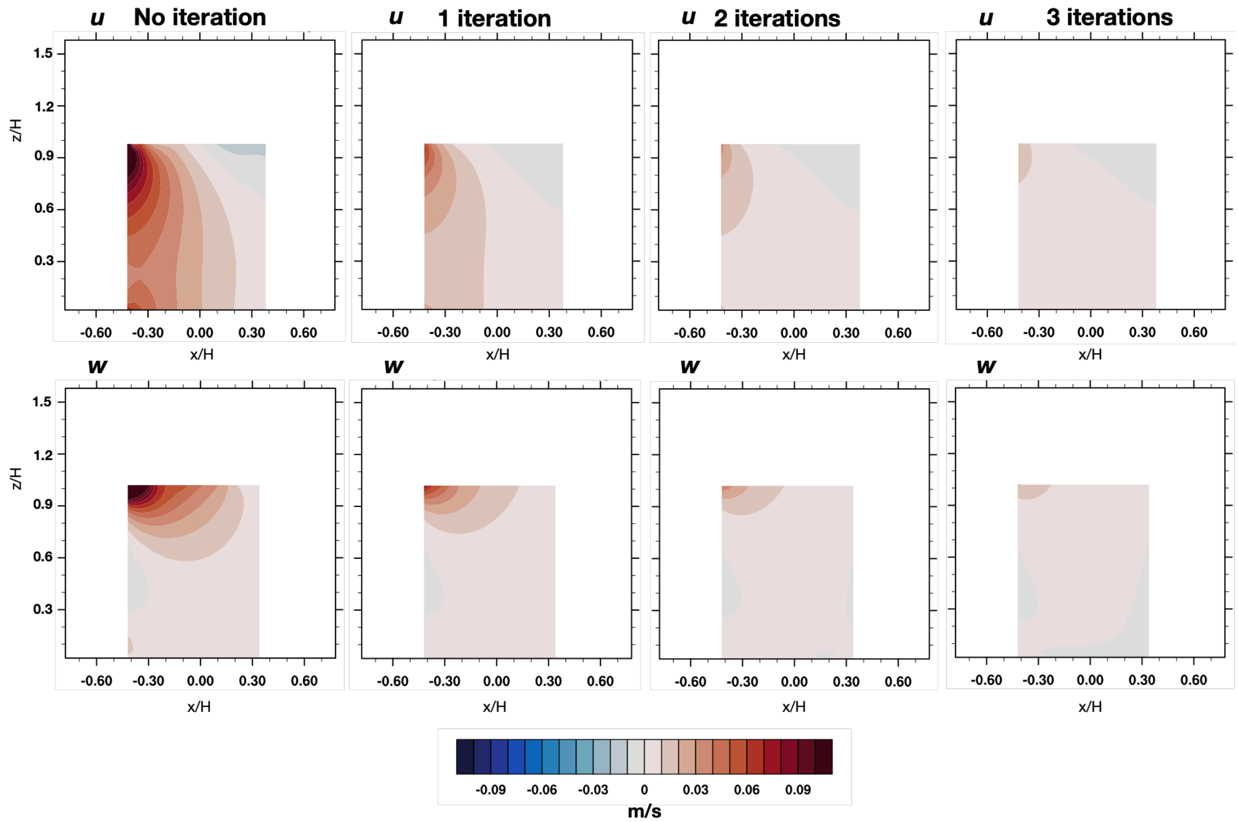

Figure 5. Residual horizonal *u* (top) and vertical w (bottom) velocities inside the building at *y/H*=0 for no additional iteration (left), and several additional iterations over the steps (5)-(8) of the QSBM as indicated above the columns.

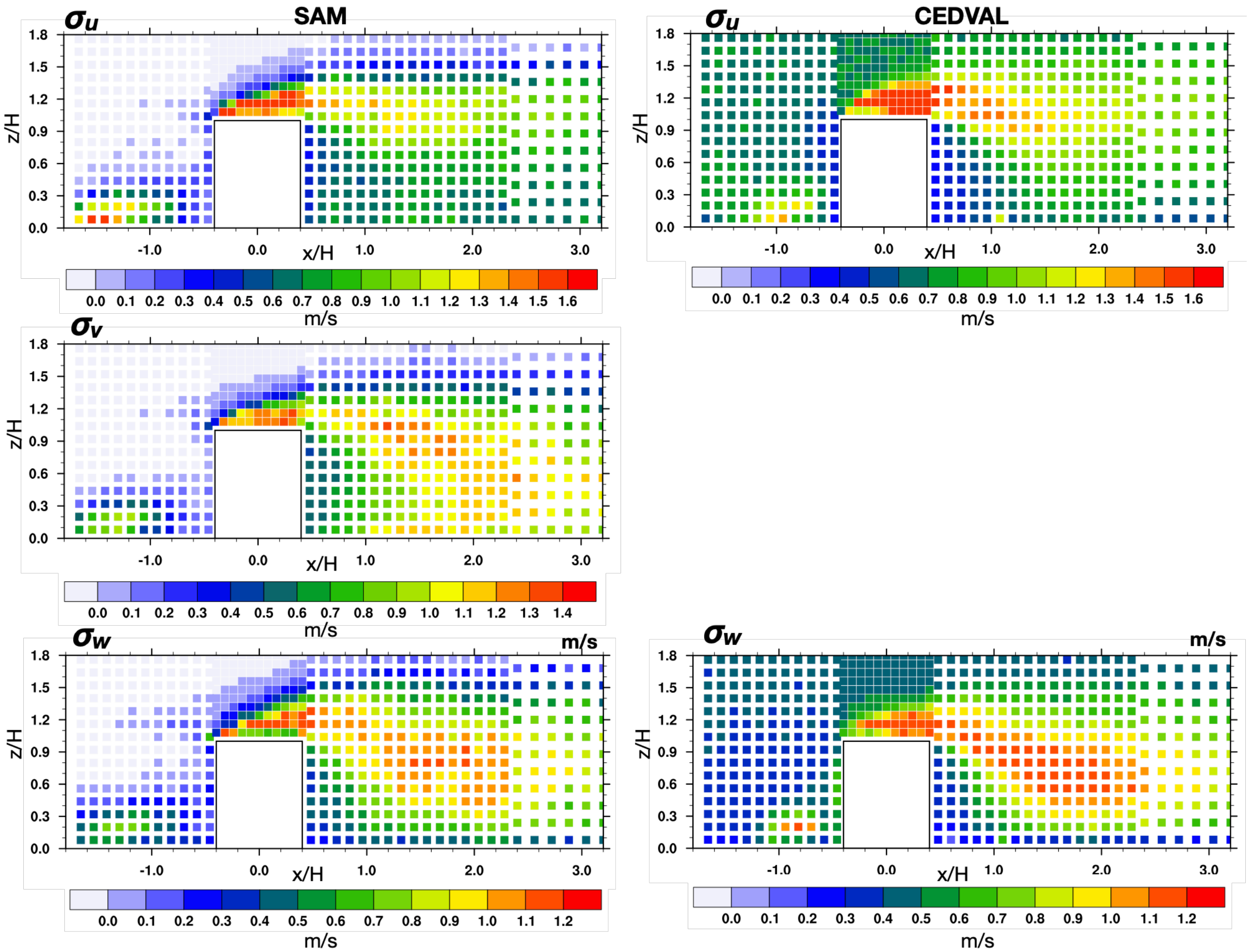

Figure 6. Turbulent intensity for different wind components at y/H=0 for SAM (left panels) and CEDVAL observations (right panels). No observations are available for *v* component. The measurement density is indicated by the discrete points plotted (i.e., no interpolation is used).

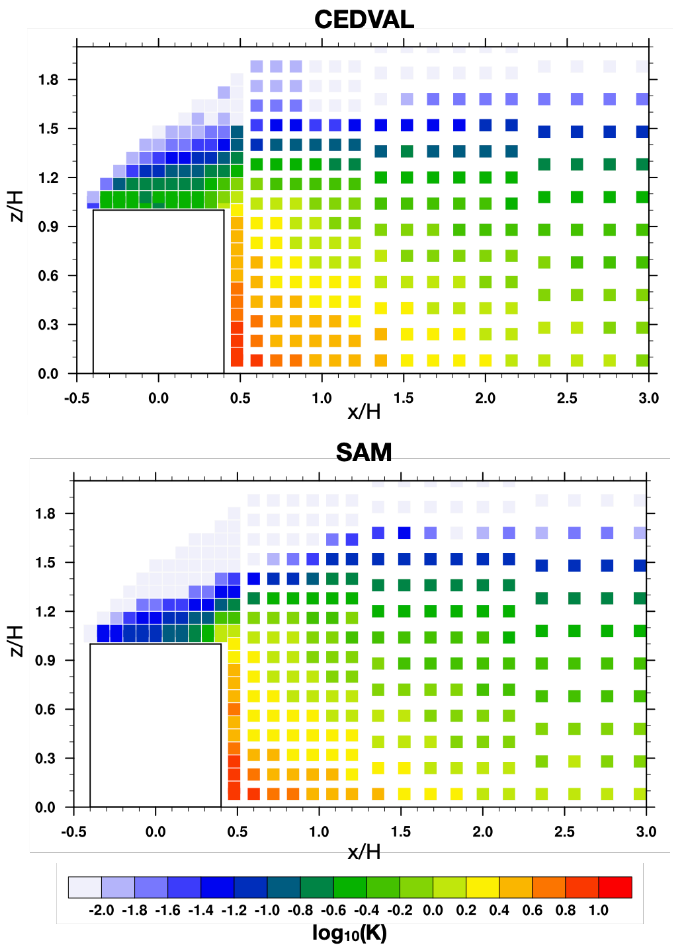

Figure 7. The dimensionless gas tracer concentration in the vertical symmetry plane *y/H*=0 for CEDVAL A1-5 observations (top) and SAM (bottom). The measurement density is indicated by the discrete points plotted (i.e., no interpolation is used).

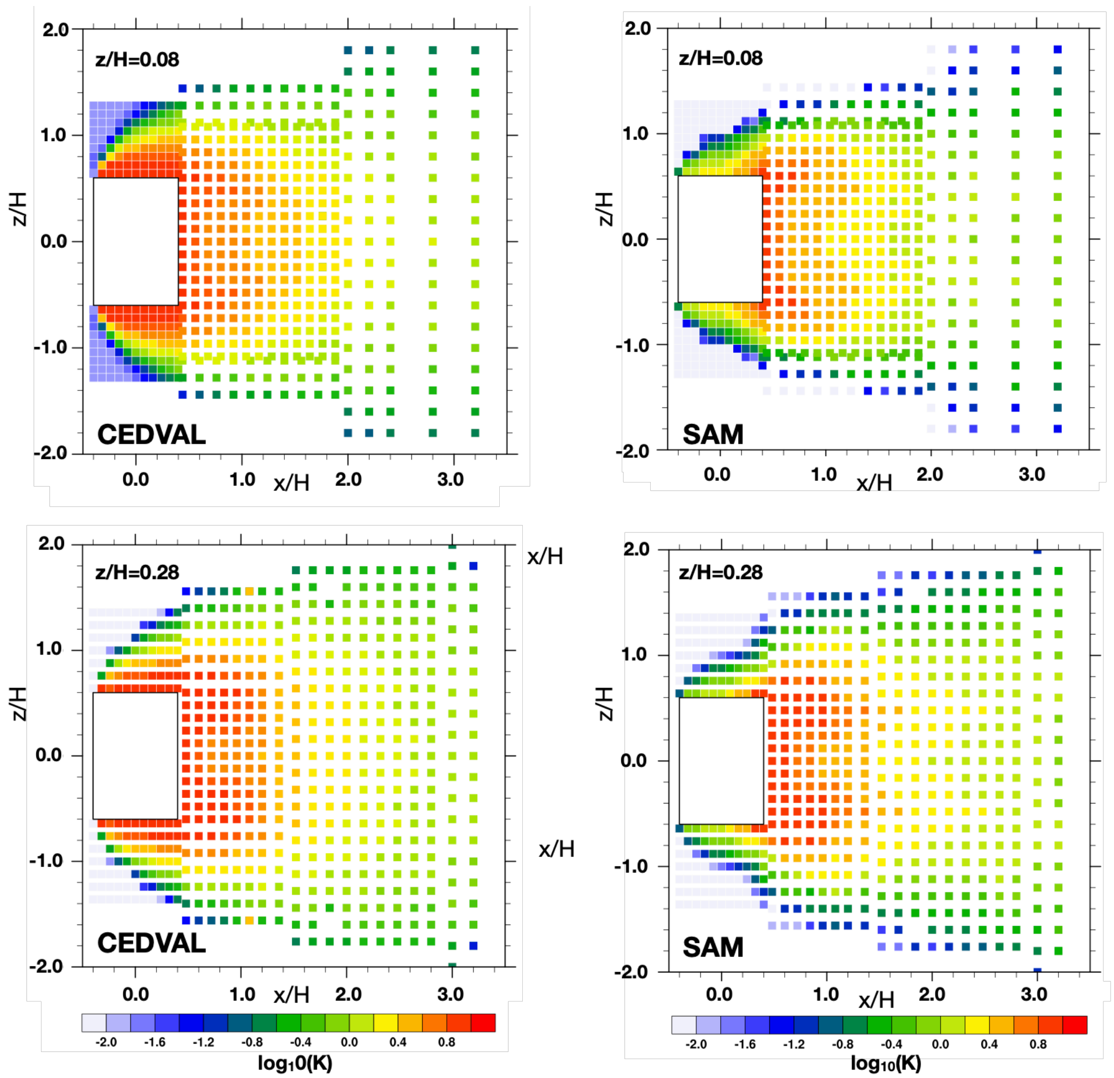

Figure 8. The dimensionless gas tracer concentration in the horizontal planes *z/H*=0.08 (top) and *z/H*=0.28 (bottom) for CEDVAL A1-5 observations (left) and SAM (right). The measurement density is indicated by the discrete points plotted (i.e., no interpolation is used).

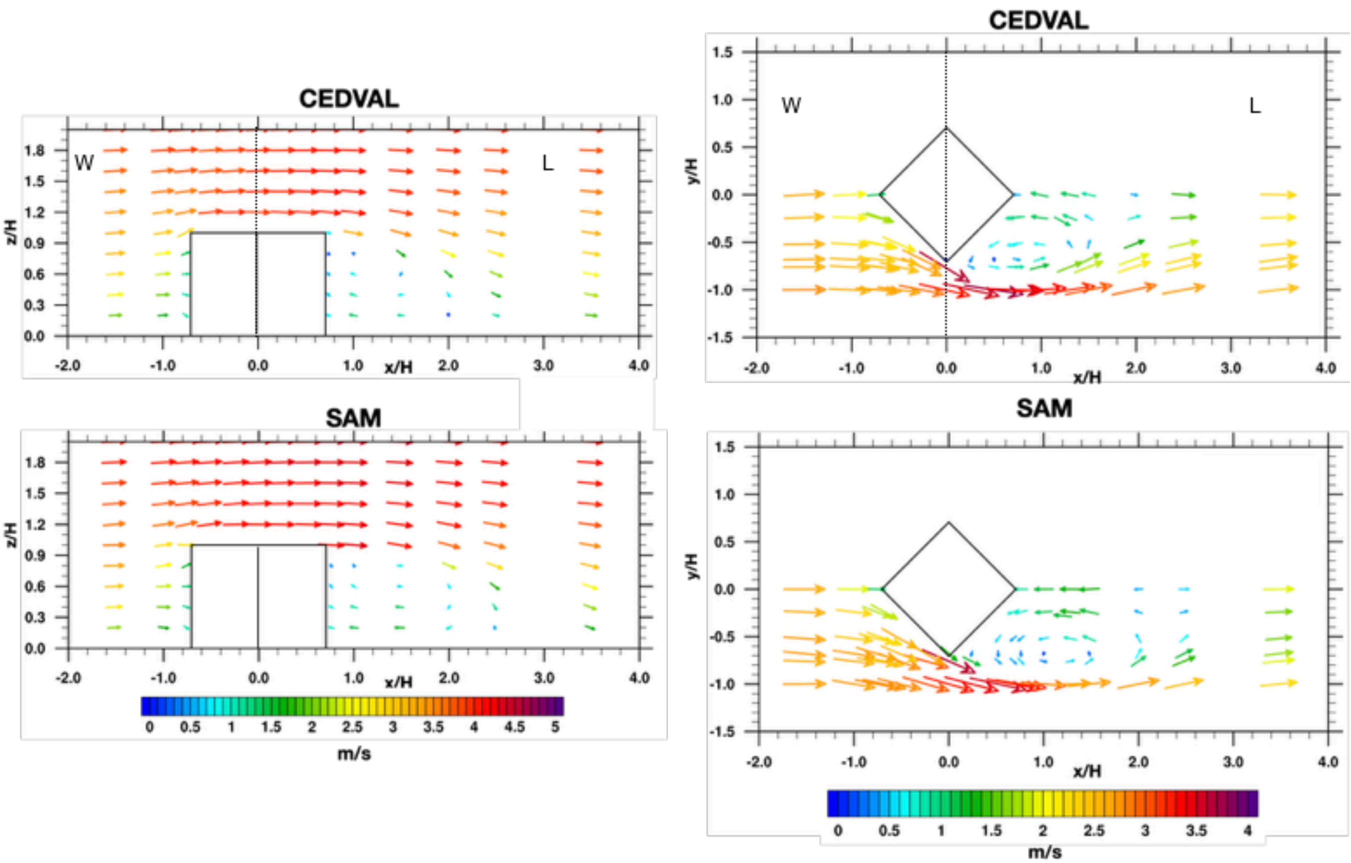

Figure 9. Vertical *x-z* cross-section at *y/H* = 0 (left panels) and horizontal *x-y* cross-section of wind at *z/H* = 0.4 (right panels) for CEDVAL A1-6 experiment (top) and SAM simulation (bottom). The coordinates are normalized by the building's height *H*. The dashed lines in the top plot indicate the boundaries of the key zones used for statistical comparison: W – windward in front of the building; L – leeside vortex and wake zone.

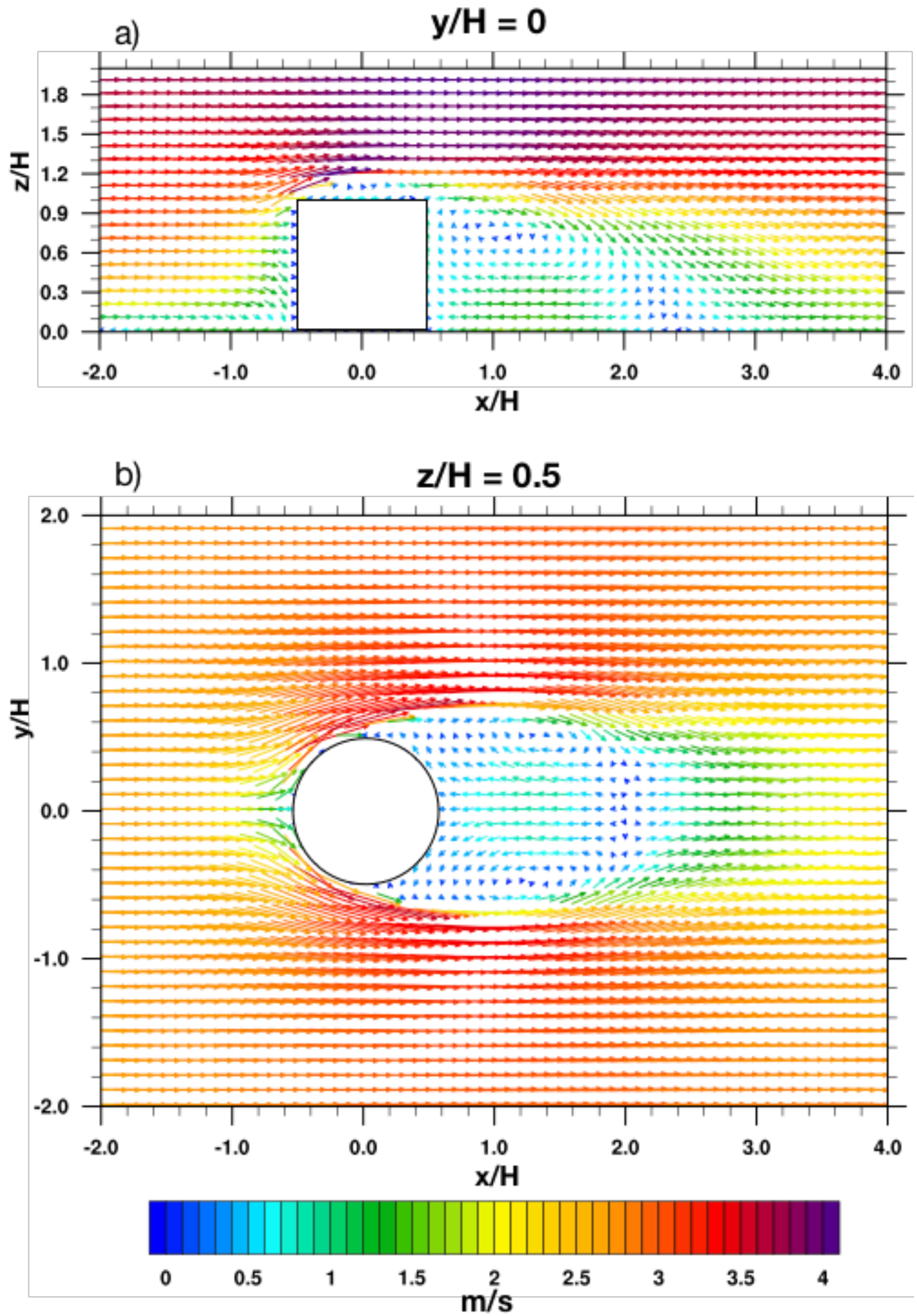

Figure 10. (a) Vertical cross-section at *y/H* = 0 and (b) horizontal cross-section at *z/H* = 0.5 of time-averaged wind for simulated flow around a cylinder with aspect ratio of one. The coordinates are normalized by height of the cylinder. The wind magnitude is shown by vector length as well as by its color.

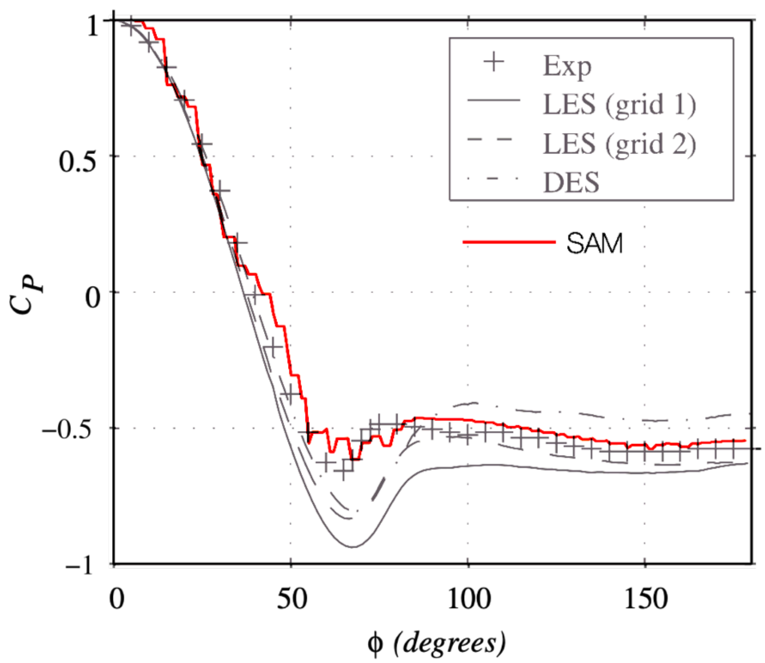

Figure 11. Pressure coefficient C_P near the surface of the cylinder as a function of cutting angle around it at z/H=0.5. Results from SAM (red line) are superimposed on Fig. 7 from Pattenden et al (2007), which shows their modeling (LES, DES) and experimental results (Exp).